Energy & Environmental Science

PAPER

View Article Online
View Journal | View Issue

Cite this: *Energy Environ. Sci.*, 2018, **11**, 383

In situ simultaneous photovoltaic and structural evolution of perovskite solar cells during film formation†

Mejd Alsari,[a] Oier Bikondoa,[b] James Bishop,[c] Mojtaba Abdi-Jalebi,[a] Lütfiye Y. Ozer,[d] Mark Hampton,[e] Paul Thompson,[f] Maximilian T. Hörantner,[i] Suhas Mahesh,[g] Claire Greenland,[c] J. Emyr Macdonald,[e] Giovanni Palmisano,[d] Henry J. Snaith,[g] David G. Lidzey,[c] Samuel D. Stranks,[a] Richard H. Friend[a] and Samuele Lilliu*[ch]

Metal-halide perovskites show remarkably clean semiconductor behaviour, as evidenced by their excellent solar cell performance, in spite of the presence of many structural and chemical defects. Here, we show how this clean semiconductor performance sets in during the earliest phase of conversion from the metal salts and organic-based precursors and solvent, using simultaneous *in situ* synchrotron X-ray and *in operando* current–voltage measurements on films prepared on interdigitated back-contact substrates. These structures function as working solar cells as soon as sufficient semiconductor material is present across the electrodes. We find that at the first stages of conversion from the precursor phase, at the percolation threshold for bulk conductance, high photovoltages are observed, even though the bulk of the material is still present as precursors. This indicates that at the earliest stages of perovskite structure formation, the semiconductor gap is already well-defined and free of sub-gap trap states. The short circuit current, in contrast, continues to grow until the perovskite phase is fully formed, when there are bulk pathways for charge diffusion and collection. This work reveals important relationships between the precursors conversion and device performance and highlights the remarkable defect tolerance of perovskite materials.

Received 19th October 2017,
Accepted 18th December 2017

DOI: 10.1039/c7ee03013d

rsc.li/ees

Introduction

Perovskite photovoltaics (PV) is one of the fastest growing optoelectronic technologies.[1–7] The ability to deposit these abundant materials with large area solution processing techniques has the potential to make perovskites viable for low-cost production.[8–10] Typical perovskite thin films in devices are fabricated by depositing mixtures of dissolved organic and inorganic precursor salts and annealing to form polycrystalline films. Despite these relatively crude solution processing methods (in comparison to methods to grow traditional inorganic solar absorbers), these materials exhibit exceptional optoelectronic properties suggesting a remarkable defect tolerance. For example, perovskite films show sharp absorption edges,[11,12] long carrier diffusion lengths[13] and high luminescence quantum efficiencies,[14] suggesting they are clean semiconductors with low densities of sub-gap trap states.[15] These properties directly translate to excellent photovoltaic figures-of-merit (FOM), with record device efficiencies currently reaching 22.1%.[7]

Researchers have investigated several engineering methods to further optimize perovskite film morphology and improve their performance.[3,16,17] Thermal engineering is the most widely studied approach, which aims to elucidate the optimal combination of annealing temperature, annealing time, atmospheric conditions and temperature profiles.[16,18–20] For most perovskite materials, the anneal temperature is critical for optimized conversion of the as-coated precursor material into

[a] *Cavendish Laboratory, University of Cambridge, CB3 0HE Cambridge, UK*
[b] *Department of Physics, University of Warwick, CV4 7AL Coventry, UK*
[c] *Department of Physics and Astronomy, University of Sheffield, Sheffield, S3 7RH, UK. E-mail: samuele_lilliu@hotmail.it*
[d] *Department of Chemical Engineering, Khalifa University of Science and Technology, Masdar Institute, PO Box 54224, Abu Dhabi, United Arab Emirates*
[e] *School of Physics and Astronomy, Cardiff University, CF24 3AA Cardiff, UK*
[f] *University of Liverpool, Oliver Lodge, Oxford Street, Liverpool, L69 7ZE, UK*
[g] *Clarendon Laboratory, Department of Physics, University of Oxford, OX1 3PU Oxford, UK*
[h] *The UAE Centre for Crystallography, United Arab Emirates*
[i] *Research Laboratory of Electronics, Massachusetts Institute of Technology, 77 Massachusetts Avenue, Cambridge, Massachusetts 02139, USA*

† Electronic supplementary information (ESI) available. See DOI: 10.1039/c7ee03013d

a crystallized perovskite film but annealing for too long may cause degradation.[16,21,22] Thus, studying how the photovoltaic performance of a perovskite solar cell evolves with time during the anneal is crucial in thermal engineering. However, to do so, one needs to pre-anneal and complete the device stack, then measure current–voltage (*JV*) sweeps *ex situ* in multiple solar cells for different annealing periods,[16,23,24] which would take an unfeasible amount of time.

In-depth complementary measurements are also needed to understand the trends of FOM profiles *vs.* annealing time. *S*ynchrotron Grazing Incidence X-ray diffraction (GI-XRD) techniques have shed light on several aspects of the precursor to perovskite conversion including degradation, phase transformations, degree of crystallinity, and distribution of crystal sizes and orientation.[16,25–31] Fast 2D detectors and high intensity X-ray beams have allowed *in situ* studies during the formation, crystallization, and degradation of perovskite films in Grazing Incidence Wide Angle X-ray Scattering (GI-WAXS) geometry.[21,22,31,32] Data obtained from *in situ* GI-XRD measurements can be used to interpret FOM profiles of perovskite solar cells *vs.* anneal time. A direct relationship between the photovoltaic performance and the structural properties can only be established when photovoltaic and structural measurements are performed simultaneously in a working solar cell. However, top layers above the perovskite film in a standard perovskite solar cell would interfere with the GI-XRD measurement when compared to a bare perovskite film, and even then it is again unfeasible to fabricate and anneal at different time periods several solar cells and then measure their diffraction patterns *ex situ*.

In this work, we explore the performance of perovskite solar cells during the formation of the perovskite from the earliest stages of its conversion from the precursor phase to the fully formed perovskite phase and during its degradation. This is achieved by leveraging the concept of interdigitated back-contact (IBC) solar cells, in which the electron and hole selective electrodes are co-positioned on the backside of the cell in an interdigitated fashion. Unlike conventional planar heterojunction solar cells, with the IBC architecture, optical transmission losses caused by the top contact can be avoided as the photoactive layer is directly exposed to light. In this work, the main advantage of IBC perovskite solar cells is that the perovskite layer represents the final step of the device fabrication. Since the perovskite film is not blocked by any capping layer, *in situ* annealing can be performed without compromising the perovskite conversion. At the same time, the perovskite film is directly accessible by an X-ray beam in GI-WAXS geometry. Here, we use the IBC structure to simultaneously acquire photovoltaic and GI-WAXS measurements *in situ* during the anneal to directly investigate the relationships between the figures-of-merit of a solar cell and its structural properties. We investigate two state-of-the-art benchmark perovskite materials for processing under ambient conditions ($MAPbI_3$, MA = methylammonium) prepared from MAI:$PbCl_2$ and two additives (HI or PbI_2). We spin-coat these solutions on the IBC architecture and show that even in the earliest stages of conversion of precursors to perovskite we achieve remarkably high open-circuit voltages, suggesting that the defect tolerance appears at an early stage in the conversion process. In contrast, the current continues to rise until the precursor conversion is complete and there is a continuous pathway for collecting charges. We show analogous trends in the FOM of planar heterojunction solar cells fabricated from MAI:$PbCl_2$ with HI and annealed *ex situ*. We further observe analogous high photovoltages before the full perovskite conversion for a variety of perovskite systems including (1) $MAPbI_3$ prepared from MAI:$PbAc_2$,[31] (2) the triple mixed cation $Cs_{0.5}(MA_{0.17}FA_{0.83})_{0.95}Pb(I_{0.83}Br_{0.17})_3$ (FA = formamidinium),[33] and (3) the mixed cation $(FAI)_{1.0}(MABr)_{0.2}(PbI_2)_{1.1}(PbBr_2)_{0.20}$.[34] Our work elucidates the direct connection between the clean semiconductor behaviour of perovskite materials and their structural properties. To the best of our knowledge, this is the first report of simultaneous photovoltaic and GI-WAXS measurements of solar cells performed *in situ* during formation of the perovskite absorber layer.

Results and discussion

We custom-designed a setup to directly monitor the structural properties of perovskite films and their photovoltaic performance during the fabrication of an interdigitated back contact (IBC) solar cell *in situ* and *in operando* (Fig. 1a). Briefly, measurements were performed at the XMaS beamline (ESRF, Grenoble, France) using an annealing chamber with regulated temperature control mounted on a diffractometer and a white LED mounted above the sample to give a similar photon flux to solar illumination conditions ($\sim$100 mW cm^{-2}) at the sample position. The substrates employed here are interdigitated ITO substrates with a channel length of 100 μm. Electron- and hole-selective electrodes were obtained by electrodepositing electrodes with TiO_2 and PEDOT, respectively (Fig. 1a).[35] The substrate was spin-coated in air with a perovskite precursor solution and immediately mounted within 20 s on the sample stage (hotplate) pre-set at a specific temperature (isothermal measurements). *JV* curves under dark and light conditions and Grazing Incidence Wide Angle X-ray Scattering (GI-WAXS) diffraction patterns under dark conditions were acquired every $\sim$54.4 s during the anneal process for $\sim$3 h. The typical measurement procedure consisted of a continuous loop of the following: (1) measure one GI-WAXS pattern (light off, X-ray on); (2) measure one current–voltage (*JV*) sweep (light off, X-ray off); (3) measure *JV* sweep (light on, X-ray off). The setup and the measurement procedure described here is also illustrated in the movie shown in ref. 52.

In Fig. 1 we show a summary of the measurements performed on an IBC solar cell spin-coated with a precursor solution made of MAI : $PbCl_2$ (2.95 : 1 M) with HI additive (1%) in dimethylformamide (DMF), which is a recipe able to produce high performance solar cells in the ambient conditions employed here.[10,36] The perovskite-coated IBC solar cell (IBC130) was annealed at 88.2 °C (measured at the sample surface) under N_2 atmosphere to minimise X-ray beam damage. The as-coated film

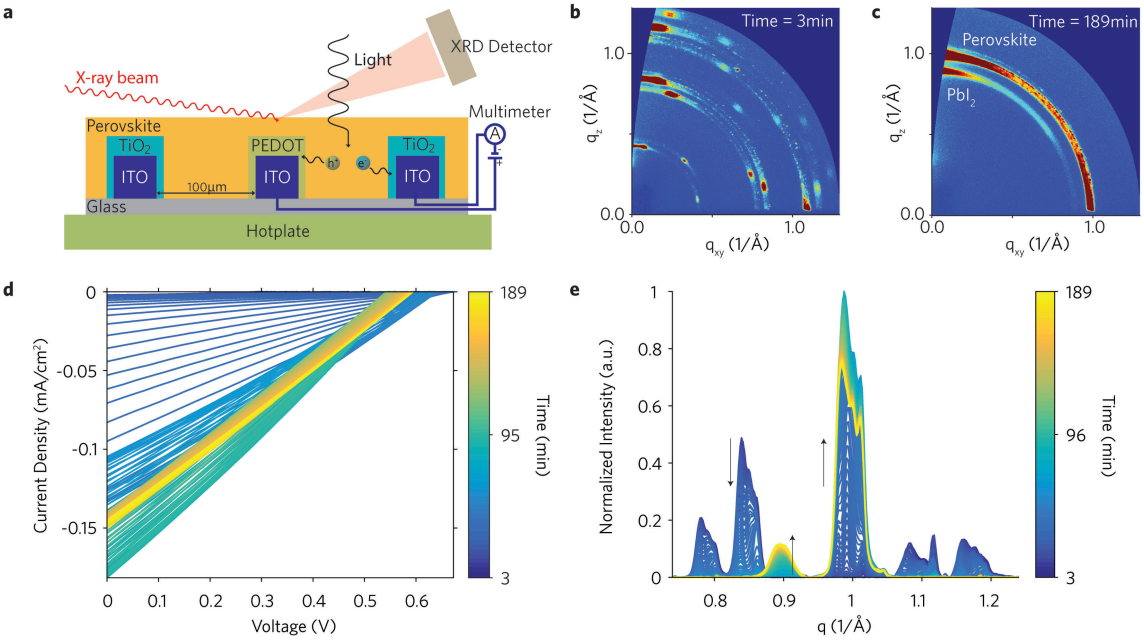

Fig. 1 Simultaneous GI-WAXS diffraction patterns and current–voltage measurement of IBC solar cell (S130) during *in situ* anneal at 88.2 °C. (a). Illustration of measurements on a perovskite IBC solar cell (the actual IBC pattern is shown in the ESI†). (b) Diffraction pattern after ~3 min from the beginning of the anneal exclusively showing the precursor phase. (c) Diffraction pattern at the end of the anneal (~189 min) showing the perovskite and the lead iodide phases. (d) IBC solar cells current–voltage sweeps measured under light. (e) Azimuthally integrated line profiles *vs.* annealing time (normalized to the maximum value of the entire dataset). The perovskite and the lead iodide peaks are located at q = 1 and 0.9 Å^{-1}, respectively. The remaining peaks belong to the precursor phase. The following measurement loop step for IBC S130 was repeated every 54.4 s: measure one GI-WAXS pattern (1 s integration time, light off), forward *JV* sweep (18 s, light off), reverse *JV* sweep (18 s, light on).

undergoes a three-stage evolution: (i) precursor phase conversion into perovskite phase, (ii) perovskite crystallization, (iii) perovskite degradation into lead iodide.[21,22,26,27] Diffraction patterns collected at the beginning of the anneal only display the characteristic crystalline precursor phase (Fig. 1b), which reaches a maximum intensity after ~15 min from the beginning of the anneal. The (100) perovskite peak, belonging to the pseudo-cubic α-phase,[37,38] gradually increases in intensity after ~10 min and reaches a maximum value after ~62 min. The primary product of the perovskite degradation, PbI_2, appears after ~70 min and increases throughout the anneal (Fig. 1c). Line profiles azimuthally integrated over the entire image are plotted in Fig. 1e and display the evolution of four precursor peaks, the perovskite peak and the PbI_2 peak in the q = [0.74 1.24] Å^{-1} range. The full sequence of GI-WAXS images and extracted data are shown in the movie for S130 shown in ref. 53.

The *JV* sweeps in Fig. 1d were performed across a 100 μm channel length. Measurements under light conditions show a rectifying behaviour and display a low photocurrent at the beginning of the anneal, with a gradual increase until ~90 min, a maximum photocurrent of 0.18 mA cm^{-2}, and a progressive reduction throughout the anneal. *JV* sweeps under dark conditions show a rectifying behaviour with negligible current density (see the movie for S130 shown in ref. 53 for a comparison between dark and light sweeps). Measurements on interdigitated ITO substrates without PEDOT and TiO_2 displayed photocurrents two orders of magnitude smaller than that of a coated device in the first 14 min of the anneal (see the movies for S28 and S29 shown in ref. 54 and Fig. S2, ESI†). However, after 14 min no photocurrent was detected. The opto-electrical properties of IBC perovskite solar cells with a channel length of 100 μm are comparable to the measurements shown in an earlier work using a channel length of 4 μm (Fig. S3, ESI†).[35] The fact that working devices can be obtained using a channel length exceeding the carriers diffusion lengths was predicted by Pazos-Outón *et al.*, who interpreted this as the effect of photon recycling, which boosts the 'diffusion' length of electrons and holes.[35] Measurements performed on IBC solar cells with gaps ranging from 50 μm to 200 μm did not show any clear trend in the FOM *vs.* channel length (Fig. S4 and S5, ESI†), suggesting that larger gaps would be required to observe clearer differences in the photovoltaic performance.

To better compare the opto-electrical measurements with the structural data, we calculate the areas under the most intense precursor peak (~0.85 Å^{-1}), the perovskite peak, and the PbI_2 peak, and plot them *vs.* the annealing time. These peak integrals represent the degree of crystallinity (*i.e.* amount of scattering crystals) of the three phases and are compared to the normalized figures-of-merit (FOM) extracted from reverse *JV* sweeps measured during the anneal in Fig. 2. Absolute values of the FOM and *JV* sweeps are available in the movie for S130 shown in ref. 53.

The short circuit current density (J_{sc}) starts from a negligible value at the beginning of the anneal (~3 min) and seems to follow a growth dynamics similar to that of the perovskite peak. It reaches a peak of 0.18 mA cm^{-2} after 90 min, decreases, and

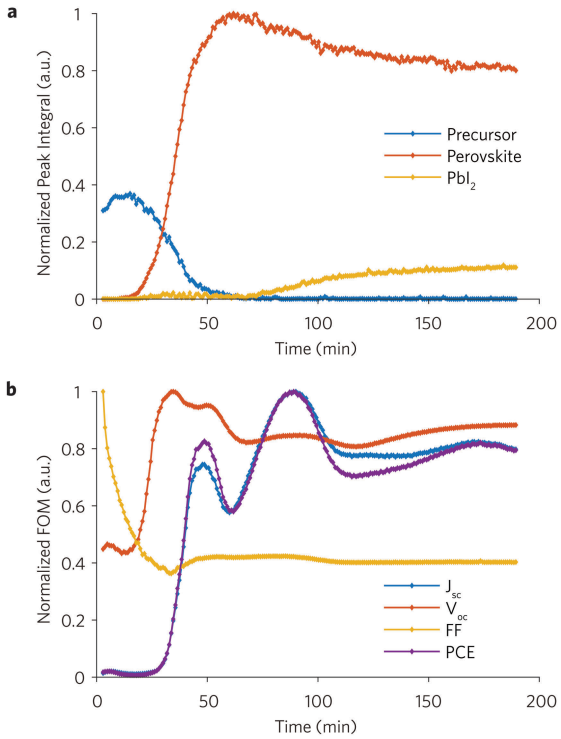

Fig. 2 Structural and opto-electrical parameters extracted from simultaneous GI-WAXS diffraction patterns (dark) and current–voltage (light) measurement of IBC solar cell (S130) during *in situ* anneal at 88.2 °C. (a) Integrated peak intensities of precursor, perovskite and PbI_2 *vs.* annealing time (b) normalized figures-of-merit (FOM) *vs.* annealing time.

settles to ~0.14 mA cm^{-2}. The open circuit voltage (V_{oc}) grows from ~0.30 V at the beginning of the anneal (~3 min) to a ~0.67 V peak after ~35 min, at which point the diffraction intensities indicate that the amount of precursor crystals is comparable to the amount of perovskite crystals. The growth of the V_{oc} takes place ~13 min earlier than the J_{sc}. After peaking, the V_{oc} progressively reduces, reaching a steady value after the precursor phase has fully converted into the perovskite phase. The fill factor (FF) sharply decreases from an initial value of 0.64 to 0.23 (~34 min), and then settles to ~0.26. The power conversion efficiency (PCE) follows a similar trend to that of the J_{sc}.

We note that the first value of the open circuit voltage (~0.30 V) is probed in the absence of any detectable diffraction signal from the perovskite phase (see Fig. 1b and 2a). A remarkably high V_{oc} (~0.52) was also measured from as-spun and un-annealed IBC solar cells measured at room temperature (see Table S2, ESI†). We further probed high V_{oc} at the beginning of the anneal of IBC solar cells (see Table S2, ESI†) spin-coated from $MAPbI_3$ prepared from MAI:$PbAc_2$,[31] a triple mixed cation system $(Cs_{0.5}(MA_{0.17}FA_{0.83})_{0.95}Pb(I_{0.83}Br_{0.17})_3)$,[33] and a mixed cation system $((FAI)_{1.0}\ (MABr)_{0.2}(PbI_2)_{1.1}(PbBr_2)_{0.20})$.[34] Although these materials are not suitable for spin-coating under ambient conditions and, therefore, performed poorly (relatively low J_{sc}) when compared with the benchmark $MAPbI_3$ materials, these tests allow us to generalise the fact that a relatively high V_{oc} can be measured in solar cells where the perovskite phase has not formed yet.

These results reveal several fascinating insights. The reasonably high voltages through many of the early stages of the conversion suggests that we have a relatively clean semiconductor from the very beginning. The moderate voltage at the start of the anneal, where we have predominantly a pure precursor phase and solvent, suggests that we first form a percolative pathway for charge transport at this earliest point in time. The photovoltage peaks at a point in time when much of the precursor material has not yet been converted to perovskite, is consistent with a self-passivation of perovskite defect states by amorphous material including precursors (PbI_2, $PbCl_2$).[39,40] The current peaks only when all of the precursors have been converted to perovskite. While the voltage peaks when surrounded by passivating dielectric material, the current only peaks when there is a continuous path for charge collection. When the current and perovskite signal peak, the perovskite grains will impinge upon each other and this is likely to introduce crystal defects at the boundaries, responsible for non-radiative recombination and hence a reduction in V_{oc}. The reduction of chloride ions (MACl), which sublimate during the precursor to perovskite conversion,[25] could be the reason why the V_{oc} reduces after reaching a peak.

To confirm whether the structural and FOM trends are interdependent, we performed analogous measurements by annealing other IBC solar cells at different temperatures: 83.8 °C (IBC S142), 92.5 °C (IBC S129), and 96.8 °C (IBC S128). Diffraction patterns, structural data, and FOM for these devices are available in the movies for S142, S129, S128 shown in ref. 55–57 and in Fig. S7–S9 (ESI†). As the annealing temperature is varied, the trend dynamics of both the FOM and the peak integrals shift together with time (Fig. S10–S13, ESI†). Particularly, the trends mentioned above for IBC S130 are also observed in IBC S142, S129, and S128. This confirms that the opto-electrical properties are directly correlated with the structural properties measured by GI-WAXS. The structural data from the IBC solar cells annealed at different temperatures can be used to assess the perovskite crystallization kinetics with the Johnson–Mehl–Avrami (JMA) model.[16,21,22] We calculate an activation energy for crystallization (~89 kJ mol^{-1}) slightly higher than the one reported by Barrows *et al.* (~85 kJ mol^{-1})[22] and by Moore *et al.* (~86 kJ mol^{-1})[21] (Fig. S14 and Table S3, ESI†). This minor difference could be due to the fact that the IBC solar cells discussed here are annealed under nitrogen atmosphere, which slows down the crystallization, and/or have HI as an additive. However, this is partially counterbalanced by the fact that the perovskite films reported here are ~200 nm thinner than the ones reported by Barrows *et al.*, which would speed up the crystallization.

The multiple oscillations in the J_{sc} and V_{oc} trends in Fig. 2b are not visible in the structural data, suggesting that they are not related to structural changes in the perovskite crystal. IBC S132 was prepared as IBC S130, with the exception that GI-WAXS and *JV* measurements were performed every 10 min, instead of every 54.4 s, corresponding to a reduction in the X-ray and light dose. As shown in the movie for S132 in ref. 58 and Fig. S15 (ESI†), a reduction in the data sampling period does not seem to mitigate the oscillations in the short circuit current density. IBC S116 was prepared as IBC 132, with the

difference that the GI-WAXS patterns were integrated for a longer period (10 s instead of 1 s) and that J_{sc} and V_{oc} were statically measured without applying any bias. In this case J_{sc} and V_{oc} appeared significantly smoother without noticeable oscillations (see the movie for S116 shown in ref. 59 and Fig. S16, ESI†). We then increased the GI-WAXS and static J_{sc} and V_{oc} sampling time on another IBC solar cell (S117) back to 54.4 s. The increased X-ray and light dose did not result in oscillations in J_{sc} and V_{oc} (see the movie for S117 shown in ref. 60 and Fig. S17, ESI†). These measurements suggest that the oscillations could be related to changes in ionic accumulation at the electrodes induced by the *JV* sweeps, potentially related to the release of excess MACl from the surface. Note that these oscillations do not affect the general trend of the figures-of-merit.

To address whether the bias applied during the *JV* sweeps could influence the dynamics of the perovskite film during the anneal, we compare the peak integrals extracted from the GI-WAXS measurements performed on IBC S132 (*JV* sweeps) and IBC S116 (static J_{sc} and V_{oc} measurements). The trends of the perovskite peak match almost perfectly in the initial phase (Fig. S19, ESI†) and thus, if any structural change takes place as an effect of the applied bias, this is not measurable with our GI-WAXS setup. After reaching a maximum value at ~63 min in IBC S116 (10 s integration time), the intensity of the perovskite peak reduces due to the higher X-ray dose.

Perovskite films can be damaged by prolonged exposure to X-rays and light. X-ray damage is visible as a yellow stripe (PbI_2) that spreads from the beam footprint position (Fig. S18, ESI†). The emergence of the PbI_2 signal and the decrease in the perovskite signal after ~70 min from the beginning of the anneal, is mainly due to beam damage (Fig. 2a), which exacerbates the natural perovskite decomposition into PbI_2 due to the loss of the organic component for extended anneal.[41] When the GI-WAXS sampling rate was reduced from one measurement every 54.4 s (IBC S130) to one measurement every 10 min (IBC S132), a much lower PbI_2 signal was recorded during the anneal. Since the X-ray beam footprint is limited to a small area of the solar cell, beam damage has a limited effect on the degradation of the figures-of-merit. However, the FOM are strongly affected by continuous exposure to light (*cf.* IBC S115 with S113 in Fig. S19, ESI†). X-ray beam and light damage are further discussed in the ESI† along with comparisons between samples exposed to different X-ray and light doses (Fig. S19, ESI†). We also find that the FOM parameters increase faster with longer light exposure over the initial periods (Fig. S19, ESI†). This is likely related to a photo-induced reduction in trap density (*i.e.* photo-brightening effects),[42] which is in turn related to photo-induced ion migration processes and could be further exaggerated with residual oxygen and moisture molecules in the precursor film.[40,43]

As already elucidated in a recent report on spray-coated and spin-coated perovskites from MAI : $PbCl_2$ (3 : 1) on both Si/SiO_2 and Si/SiO_2/PEDOT:PSS substrates, the annealing process is characterized by the rotation and lattice contraction and expansion of both perovskite and precursor crystallites.[27] The grain evolution is evident from the change in the scattering vector position of the diffraction spots populating the diffraction rings of the GI-WAXS patterns during the *in situ* anneal.[27] From the sequences of GI-WAXS images of all the IBC solar cells reported in this work (see the movie shown in ref. 52) we observe again that the diffraction spots from single crystallites move in the reciprocal space during the anneal, which is an indication of grain rotation and lattice contraction/expansion. By reducing the sampling rate from 54.4 s down to 11 s (see the movie for S131 shown in ref. 61) the moving diffraction spots can be observed in a clearer way.

To establish whether IBC solar cells fabricated and measured *in situ* during the anneal show performance dynamics similar to standard solar cells fabricated *ex situ*, we prepared a series of planar heterojunction solar cells and annealed them *ex situ* for different periods. Compact TiO_2 was deposited *via* spray-pyrolysis onto FTO substrates, followed by a spin-coated TiO_2 mesoporous layer. The perovskite layer was spin-coated onto this mesoporous layer and annealed at ~97 °C for various periods (1–180 min). Doped (Li-TFSi and *t*BP) Spiro-OMeTAD was spin-coated onto the perovskite layer before an 80 nm gold electrode was thermally evaporated.

Fig. 3a shows a comparison between the normalized J_{sc} of the planar solar cells and two IBC solar cells annealed at ~97 °C. On the first IBC device (S128) we performed simultaneous electrical measurements and GI-WAXS measurements every 54.4 s. The electrical measurements consisted of a forward *JV* sweep under dark (18 s) followed by a reverse *JV* sweep under light (18 s). In the GI-WAXS measurement under dark the IBC was exposed to the X-ray beam for 1 s. On the second IBC device (S105) we performed static J_{sc} and V_{oc} measurements under light (6 s), without applying any bias and without exposing the IBC to the X-ray beam. The J_{sc} follows the same initial trend for the two architectures and reaches a peak after 20–30 min. This peak roughly corresponds to the instant when the perovskite film has fully converted and reached the maximum crystallization point (Fig. 3c). The first IBC device (S128) undergoes a sudden drop in the J_{sc} after 22 min caused by a relatively high light dose. We observe an analogous but less pronounced decay in the second IBC device (S105) thanks to the lower light dose and the absence of applied bias. The planar solar cells show a relatively stable performance after the first 20 min. Prolonged annealing for 3 hours shows no statistically significant reduction in performance (see absolute values in Fig. S20, ESI†). As discussed above, trends similar to the ones displayed by the planar solar cells were observed in IBC solar cells by reducing the J_{sc} and V_{oc} sampling rate to 10 min (IBC S142, S130, S129). However, this data is only available for lower temperatures.

Fig. 3b shows a comparison between the normalized V_{oc} of the planar solar cells and the two IBC solar cells annealed at ~97 °C. The three profiles all show a relatively high open circuit voltage at the beginning of the anneal similarly to what we observed in the earlier discussion. In the first IBC solar cell (S128) the V_{oc} shows a trend that is similar to the J_{sc}, although it reaches a peak when the peak intensity of the precursor phase

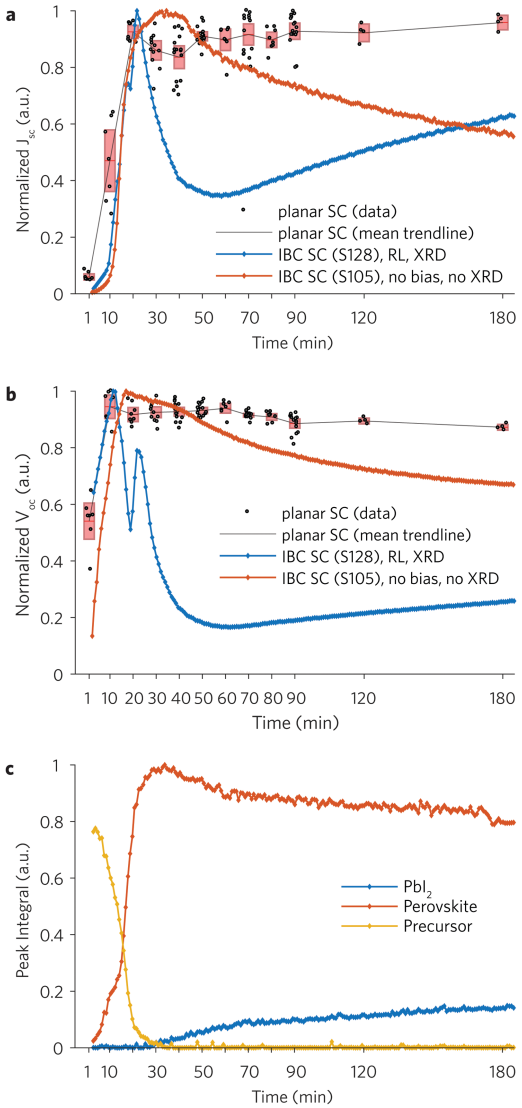

Fig. 3 Normalized short circuit current and open circuit voltage of IBC solar cells annealed *in situ* and planar heterojunction solar cells annealed *ex situ* at ~97 °C and structural data. (a) Comparison between normalized J_{sc} of two IBC solar cells (SC) and a series of planar solar cells. The red bars indicate the average ± std for the data points (black dots). The following measurement procedure for S128 was repeated every 54.4 s: measure one GI-WAXS pattern (1 s integration time), forward *JV* sweep (18 s, light off), reverse *JV* sweep (18 s, light on, indicated as RL). The following measurement procedure for S105 was repeated every 54.4 s: wait 47.8 s with the light off, measure J_{sc} (3 s light on), measure V_{oc} (3 s light on). (b) Normalized V_{oc} (see a). (c) Normalized GI-WAXS integrated intensity of the PbI_2, perovskite peak, and precursor peak extracted from the azimuthally integrated line profiles. The GI-WAXS data was acquired *in operando* during the annealing of the IBC solar cell S128.

equals the intensity of the perovskite phase (Fig. 3b). The FF in the IBC solar cells behaves in a very different way compared to the planar solar cells, and is characterized by a sudden drop within the first 10 min of the anneal (Fig. S21, ESI†). The PCE of the IBC and planar devices shows a trend that is similar to the J_{sc} (Fig. S22, ESI†).

Although the scope of this work is not to fabricate IBC solar cells that can compete with planar solar cells, the absolute values of the figures-of-merit of the IBC solar cells (Fig. S20, ESI†) are significantly lower than that of the planar solar cells (see ref. 52). This is due to a variety of factors including limits in the carrier selectivity of PEDOT and TiO_2, goodness of the electrodeposition, the fact that measurements are performed at high temperature,[44,45] and different device architectures. More selective interlayers and shorter electrodes distances could improve the efficiency of IBC solar cells.

The illustrated measurements suggest that the figures-of-merit of IBC solar cells fabricated and measured *in situ* during the anneal follow dynamics comparable to that of standard planar solar cells. This implies that IBC solar cells can provide a fast and low-cost route for optimizing perovskite materials requiring thermal annealing treatments, while preserving the features of the standard solar cells. The dataset presented for the planar solar cells is the result of the fabrication of 40 devices, each made of 4 usable pixels, *i.e.* solar cells. The time required for the entire fabrication and measurements was about 30 h. This was necessary to provide acceptable statistics, resulting in reasonably smooth trends of the average values of the figures-of-merit. We can imagine that such a trend would represent the behaviour of a hypothetical planar solar cell measured *in situ* during the anneal. On the other hand, the fabrication and measurement of a single IBC solar cell would require ~3.5 h. The figures-of-merit extracted *in situ* are clearly smoother than the ones extracted for the planar solar cells, because adjacent points of the trend lines are measured on the same device. Furthermore, the integration of simultaneous GI-WAXS measurements with the opto-electrical measurements of IBC solar cells fabricated *in situ* during the anneal, gives the opportunity to relate the figures-of-merit to the structural properties. We note that we also see similar results for our IBC devices when fabricated using a different precursor route ($MAI:PbCl_2$ with PbI_2 additive), suggesting that the results we show can be generalised (see Fig. S23 and ESI† for discussion).

Conclusion

In summary, we investigate the performance of perovskite solar cells during the formation of the perovskite starting from the earliest stages of its conversion from the precursors and solvent to the fully formed perovskite and during its degradation employing simultaneous Grazing Incidence Wide Angle X-ray Scattering and current–voltage measurements on films annealed *in situ* and deposited on interdigitated back-contact substrates. This suite of analyses allows establishing a direct correlation between the crystallographic and photovoltaic properties of working solar cells. The remarkably clean semiconductor behaviour of perovskites is evidenced by the high photovoltages measured at the first stages of perovskite conversion from precursors, at the percolation threshold for bulk conductance. Open circuit voltages reach maximum value before the precursor has fully converted into perovskite, when the fraction of precursor and perovskite crystals are comparable. Short circuit currents and power conversion efficiencies follow a trend similar to that of the perovskite

peak intensity extracted from the GI-WAXS measurements. We have shown that the behaviour of the figures-of-merit *versus* annealing time of IBC devices compares well with analogous profiles of conventional planar heterojunction solar cells, and that our results can be generalised to other perovskite precursor routes. The measurement strategy followed in this work is not limited to perovskite materials and will be of interest for any solution processable photovoltaic technology requiring thermal annealing.

Materials and methods

IBC substrates

Interdigitated ITO substrates were purchased from Ossila Ltd (code S162) and were sonicated in acetone and isopropanol and dried with N_2. The TiO_2 and polyethylenedioxythiophene (PEDOT) electrodeposition were performed in a similar manner as already reported in Pazos-Outón *et al.*[35] The TiO_2 electrodeposition on electrodes 6–10 (see Fig. S1, ESI†) was done in a single compartment using three-electrode electrochemical cell consisting of an Ag/AgCl reference electrode, a Pt counter electrode, and the ITO substrate as the working electrode.[46] The deposition bath contained 0.01–1 M of $TiOSO_4$ (Sigma-Aldrich), H_2O_2 (Sigma-Aldrich) and NH_4NO_3 (Sigma-Aldrich), and was kept at a temperature of 10 °C.[47] Crystalline anatase TiO_2 films were obtained by applying −1.05 V for 800 s (*versus* Ag/AgCl) and subsequently heating the coated substrates at 300 °C for 1 h in air. On the remaining ITO electrodes (1–5), PEDOT was deposited through electropolymerisation using a three-electrode configuration consisting of an Ag pseudo-reference electrode, a Pt counter electrode, and the ITO substrate as the working electrode.[48] The deposition bath consisted of a solution 0.01 M 3,4-ethylenedioxythiophene (EDOT) monomer (Sigma-Aldrich) in 1.0 M of $LiClO_4$ (Acros Organics) electrolyte in propylene carbonate (Sigma-Aldrich). The anodic polymerisation was carried out at 1.25 V (*versus* Ag) for 1 s.

Perovskite precursor solutions

MAI:$PbCl_2$ + HI. The perovskite precursor solution consisted of a blend between 395 mg of CH_3NH_3I (MAI) and 234 mg of $PbCl_2$ (2.95 : 1 mol), diluted in DMF (630 mg mL^{-1}). Hydrogen iodide (HI) was added into the solution (1 vol%). Addition of HI results in continuous perovskite films and more efficient solar cells compared to bare MAI:$PbCl_2$.[10,36] The as-prepared solution was used for preparing the planar solar cells, however the IBC solar cells required a much thinner perovskite layer. For this reason, the solution was further diluted twice in DMF. The final perovskite solution was filtered and kept at 70–75 °C prior to spincoating. For the planar solar cells the solution was spincoated at 2000 rpm for 45 s under ambient conditions. For the IBC solar cells the solution was spincoated onto a pre-heated substrate (from a hotplate at 100 °C) at 2000 rpm for 45 s under ambient conditions.

MAI:$PbCl_2$ + PbI_2. MAI : $PbCl_2$ (3 : 0.98 mol) with PbI_2 (0.5 vol%) was dissolved in DMF (42.2 wt%). The solution was diluted twice in DMF and spin-coated at 2000 rpm for 45 s under ambient conditions. The presence of a trace amount of PbI_2 induces a homogenous distribution of $MAPbI_3$ seed crystals during the film formation. The seeds subsequently grow to yield a highly crystalline film with enhanced optoelectronic properties.[49]

MAI : $PbAc_2$. MAI : $PbAc_2$ (3 : 1 mol) was dissolved in DMF (40 wt%) (all materials were purchased from Sigma-Aldrich or Acros Organics and were used as received).[31] The perovskite solution was spincoated at 2000 rpm for 60 s under ambient conditions.

$Cs_{0.5}(MA_{0.17}FA_{0.83})_{0.95}Pb(I_{0.83}Br_{0.17})_3$. The organic cations were purchased from Dyesol; the lead compounds from TCI; Dimethylformamide (DMF), cesium iodide from Sigma Aldrich. The triple cation lead mixed halide perovskite precursor solution was prepared by dissolving 1 M FAI, 1.1 M PbI_2, 0.2 M MABr, 0.2 M $PbBr_2$ in a 4 : 1 (v : v) mixture of anhydrous DMF : DMSO and 1.5 M stock solution of CsI in DMSO was added to above solution in 5 : 95 volume ratio.[33] The perovskite solution was then spin coated at 6000 rpm 30 s under ambient conditions. During the second step, 50 μL of chlorobenzene was dripped on the spinning substrate 10 s prior the end.

$(FAI)_{1.0}(MABr)_{0.2}(PbI_2)_{1.1}(PbBr_2)_{0.20}$. The organic cations were purchased from Dyesol; the lead compounds from TCI; dimethylformamide (DMF), cesium iodide from Sigma Aldrich. The mixed cation lead mixed halide perovskite precursor solution[34] was prepared by dissolving FAI (215 mg), MABr (28 mg), PbI_2 (634 mg), $PbBr_2$ (92 mg) in a 4 : 1 (v : v) mixture of anhydrous DMF : DMSO. The perovskite solution was then spin coated in two steps: 1000 rpm for 10 s followed by 6000 rpm for 35 s under ambient conditions. During the second step, 70 μL of anisole was dripped on the spinning substrate 5 s prior the end.

Planar heterojunction solar cells fabrication and characterization

TEC 8 and 10 glass substrates (XOP glass) were etched with zinc powder and 4 M HCl prior to sonication in Helmanex detergent solution, deionised water, and IPA. Substrates were transferred to a hotplate and heated to 450 °C for spray pyrolysis of compact titanium oxide. 1.72 mL of titanium diisopropoxide bis(acetylacetonate) (Sigma 325252) was diluted with IPA to 20 mL. This solution was then sprayed onto the substrates *via* a handheld spray gun (Draper 09709) with a nitrogen feed at 30 psi. Substrates were coated every 30 s until all the precursor was used and left to sinter for 30 min. Dyesol 18-NRT mesoporous paste was diluted to 22% weight in ethanol and spin coated onto the substrates at 2000 rpm. These were then transferred to a hotplate to be sintered for 1 h at 450 °C. The perovskite ink was prepared and spin-coated as described above. Spiro-OMeTAD solution (Ossila) was prepared at a concentration of 96.6 mg mL^{-1} in chlorobenzene. This solution was then doped with the following quantities of dopant per 1 mL of spiro-OMeTAD solution: 30 μL Li-TFSi (175 mg mL^{-1} in acetonitrile), 10 μL *t*BP, and 20 μL of FK-209 (175 mg mL^{-1} in acetonitrile). The doped spiro-OMeTAD solution was then spin coated at 2000 rpm onto the annealed perovskite films. Finally, an 80 nm gold electrode was

evaporated in an Edwards Auto 306 bell-jar evaporator at a pressure of $\sim 10^{-6}$ mbar. All solution-processed layers were deposited under ambient conditions. Devices were characterised by measuring *JV* curves with a Keithley 237 source measure unit under AM 1.5 simulated solar irradiance (Newport 92251A-1000). Each device consisted of six 4 mm^2 pixels. Due to defects associated with edge pixels these were ignored leaving four usable pixels per device. Devices were illuminated through a shadow mask with an aperture of 0.026 cm^2 and scanned from -1.2 V to 1.2 V at a speed of 0.4 V s^{-1}. Performance metrics were calculated from the reverse scan.

Beamline setup

The beamline setup illustrated here represents an evolution of the setup detailed in ref. 27. A fixed-exit, water-cooled, double crystal Si(111) monochromator was used to monochromatize the X-ray beam coming from a bending magnet (E_c = 9.8 keV).[27] The X-ray energy was tuned to 10 keV (1.2398 Å) and a Rh-coated toroidal mirror was used to focus the monochromatic beam horizontally and vertically. The beam flux was $\sim 5 \times 10^{10}$ photons s^{-1} at the sample position.[27] The original beam spot size was 500 (horizontal) × 400 (vertical) μm^2 at the sample position.[27] We employed a set of motorized slits (Huber, Germany) immediately before the sample to have a better defined footprint in the vertical direction.[27] The final beam spot size with slits was 300 (horizontal) × 115 (vertical) μm^2. The beam footprint extended 300 μm horizontally and throughout the entire length of the IBC substrate.

Annealing chamber

The sample stage consists of a thin polished copper hotplate. A temperature controller regulates the hotplate temperature with a thermocouple mounted on its surface and two cartridge heaters. On top of the hotplate, a polyether ether ketone (PEEK) structure holds two gold plated screws acting as electrical probes, which are connected to a multimeter. The electrical contacts pressing against the IBC substrate provided mechanical stability and good thermal contact with the hotplate. A white LED is mounted on the ceiling of the annealing chamber at about 6 cm from the sample stage giving a similar photon flux to solar illumination conditions ($\sim$100 mW cm^{-2}) at the sample position. The annealing chamber is illustrated in Fig. S1 (ESI†) and in the movie shown in ref. 52.

X-Ray measurements

The IBC substrate coated with PEDOT and TiO_2 was mounted on the hotplate preset at a specific temperature. The temperature was not changed during the measurements. The hotplate was pre-aligned with an IBC substrate before the actual device was mounted on it. The polished hotplate and the pressure exerted by the electrical probes on the substrate allowed keeping a good and repeatable alignment. However, because the actual device was not aligned small deviation from the actual incident angle could be present. While this has a negligible effect on GI-WAXS measurements, it has prevented us from performing GI-SAXS measurements, where small misalignments greatly affect the measured diffraction patterns. The time between the end of the spin-coating and the beginning of the GI-WAXS and *JV* measurements was about $\sim$3 min, and therefore data between 0 and $\sim$3 min is not available in the plots shown in this work. Measurements were performed at an out-of-plane incident angle of $\alpha_i \approx 0.3^\circ$ corresponding to a penetration depth of $\sim$140 nm.[50]

Current–voltage sweeps

Current–voltage sweeps were performed with a Keithley 2401 source meter. Forward and reverse *JV* sweeps were performed from -0.2 V to 1 V, and from 1 V to -0.2 V, respectively. In both cases the voltage step was 0.01 V, resulting in 120 points per sweep. At each voltage step, the bias was held constant for 50 ms (delay) before measuring the current. Solar cells were not pre-biased before the *JV* sweep. The power of the white LED used for the *JV* sweeps under illumination was tuned with an irradiance meter (91159V, Newport, USA) to give an approximate irradiance of 100 mW cm^{-2}. The *JV* sweeps and the light switch were remotely controlled *via* a SPEC macro from the beamline control cabin. For the calculation of the short circuit current and the PCE we employed an active area of 0.0396 cm^2, defined by the total area of the interdigitated electrodes facing each other (Fig. S32, ESI†).

X-ray diffraction analysis

Data processing was performed with the MATLAB software (GI-WAXS GUI) described in our previous works.[27,51] Azimuthally integrated line profiles were extracted from the 'cake slice' between $\chi = 7^\circ$ to $\chi = 89^\circ$ in steps of $\sim 0.51^\circ$ (160 line profiles at different χ) (Fig. S33, ESI†). In order to obtain an accurate estimate of the peak integrated intensities, we first removed the baseline from line profiles and then fitted the precursor, perovskite, and PbI_2 with multiple Gaussians. The peak integrals discussed throughout the text are the integrals of the fitted peaks.

Author contributions

M. A. and S. L. conceived the experiments. M. A. fabricated the IBC substrates, performed the measurements at the beamline, and analysed the data. O. B. took care of the setup at the beamline. J. B. fabricated the planar solar cells. J. B., M. A. J., M. H., S. M. prepared the precursor solutions. M. A. J. helped optimizing the electrodes deposition and precursor solution concentration. L. Y. O., M. H., J. E. M., and C. G. helped with the measurements at the beamline. P. T. designed a key component of the annealing chamber. S. L. was the main investigator of the measurements at the synchrotron, managed the project, and wrote the software for the data analysis. All authors discussed the results and contributed to the manuscript.

Conflicts of interest

There are no conflicts to declare.

Acknowledgements

This work was funded by 'The President of the UAE's Distinguished Student Scholarship Program (DSS), granted by the Ministry of Presidential Affairs, UAE' (M. A. PhD scholarship). S. L. obtained funding for the synchrotron measurements. XMaS is a mid-range facility supported by the Engineering and Physical Sciences Research Council (EPSRC). We are grateful to all the XMaS beamline team staff for their support. D. G. L. obtained the following funding from the EPSRC: J. B. PhD scholarship *via* the University of Sheffield DTG account and C. G. PhD scholarship from the Centre for Doctoral Training in New and Sustainable PV, EP/L01551X/1. M. A. J. gratefully acknowledges Nava Technology Limited and Nyak Technology Limited for a PhD scholarship. S. D. S. has received funding from the European Union's Seventh Framework Programme (Marie Curie Actions) under REA grant number PIOF-GA-2013-622630.

Notes and references

1 M. Liu, M. B. Johnston and H. J. Snaith, Efficient planar heterojunction perovskite solar cells by vapour deposition, *Nature*, 2013, **501**(7467), 395–398.
2 H. Zhou, Q. Chen, G. Li, S. Luo, T.-b. Song and H.-S. Duan, *et al.*, Interface engineering of highly efficient perovskite solar cells, *Science*, 2014, **345**(6196), 542–546.
3 N. J. Jeon, J. H. Noh, Y. C. Kim, W. S. Yang, S. Ryu and S. I. Seok, Solvent engineering for high-performance inorganic–organic hybrid perovskite solar cells, *Nat. Mater.*, 2014, **13**(9), 897–903.
4 N. J. Jeon, J. H. Noh, W. S. Yang, Y. C. Kim, S. Ryu and J. Seo, *et al.*, Compositional engineering of perovskite materials for high-performance solar cells, *Nature*, 2015, **517**(7535), 476–480.
5 H.-S. Kim, C.-R. Lee, J.-H. Im, K.-B. Lee, T. Moehl and A. Marchioro, *et al.*, Lead Iodide Perovskite Sensitized All-Solid-State Submicron Thin Film Mesoscopic Solar Cell with Efficiency Exceeding 9%, *Sci. Rep.*, 2012, **2**, 591.
6 M. M. Lee, J. Teuscher, T. Miyasaka, T. N. Murakami and H. J. Snaith, Efficient Hybrid Solar Cells Based on Meso-Superstructured Organometal Halide Perovskites, *Science*, 2012, **338**(6107), 643–647.
7 W. S. Yang, B.-W. Park, E. H. Jung, N. J. Jeon, Y. C. Kim and D. U. Lee, *et al.*, Iodide management in formamidinium-lead-halide-based perovskite layers for efficient solar cells, *Science*, 2017, **356**(6345), 1376–1379.
8 A. T. Barrows, A. J. Pearson, C. K. Kwak, A. D. Dunbar, A. R. Buckley and D. G. Lidzey, Efficient planar heterojunction mixed-halide perovskite solar cells deposited *via* spray-deposition, *Energy Environ. Sci.*, 2014, **7**(9), 2944–2950.
9 K. Hwang, Y. S. Jung, Y. J. Heo, F. H. Scholes, S. E. Watkins and J. Subbiah, *et al.*, Toward Large Scale Roll-to-Roll Production of Fully Printed Perovskite Solar Cells, *Adv. Mater.*, 2015, **27**(7), 1241–1247.
10 D. K. Mohamad, J. Griffin, C. Bracher, A. T. Barrows and D. G. Lidzey, Spray-Cast Multilayer Organometal Perovskite Solar Cells Fabricated in Air, *Adv. Energy Mater.*, 2016, **6**(22), DOI: 10.1002/aenm.201600994.
11 S. De Wolf, J. Holovsky, S.-J. Moon, P. Löper, B. Niesen and M. Ledinsky, *et al.*, Organometallic Halide Perovskites: Sharp Optical Absorption Edge and Its Relation to Photovoltaic Performance, *J. Phys. Chem. Lett.*, 2014, **5**(6), 1035–1039.
12 A. Sadhanala, F. Deschler, T. H. Thomas, S. E. Dutton, K. C. Goedel and F. C. Hanusch, *et al.*, Preparation of Single-Phase Films of $CH_3NH_3Pb(I_{1-x}Br_x)_3$ with Sharp Optical Band Edges, *J. Phys. Chem. Lett.*, 2014, **5**(15), 2501–2505.
13 S. D. Stranks, G. E. Eperon, G. Grancini, C. Menelaou, M. J. P. Alcocer and T. Leijtens, *et al.*, Electron-Hole Diffusion Lengths Exceeding 1 Micrometer in an Organometal Trihalide Perovskite Absorber, *Science*, 2013, **342**(6156), 341–344.
14 F. Deschler, M. Price, S. Pathak, L. E. Klintberg, D.-D. Jarausch and R. Higler, *et al.*, High Photoluminescence Efficiency and Optically Pumped Lasing in Solution-Processed Mixed Halide Perovskite Semiconductors, *J. Phys. Chem. Lett.*, 2014, **5**(8), 1421–1426.
15 S. D. Stranks, Nonradiative Losses in Metal Halide Perovskites, *ACS Energy Lett.*, 2017, **2**(7), 1515–1525.
16 V. L. Pool, B. Dou, D. G. Van Campen, T. R. Klein-Stockert, F. S. Barnes and S. E. Shaheen, *et al.*, Thermal engineering of $FAPbI_3$ perovskite material *via* radiative thermal annealing and in situ XRD, *Nat. Commun.*, 2017, **8**, 14075.
17 W. S. Yang, J. H. Noh, N. J. Jeon, Y. C. Kim, S. Ryu and J. Seo, *et al.*, High-performance photovoltaic perovskite layers fabricated through intramolecular exchange, *Science*, 2015, **348**(6240), 1234–1237.
18 A. Dualeh, N. Tétreault, T. Moehl, P. Gao, M. K. Nazeeruddin and M. Grätzel, Effect of Annealing Temperature on Film Morphology of Organic–Inorganic Hybrid Pervoskite Solid-State Solar Cells, *Adv. Funct. Mater.*, 2014, **24**(21), 3250–3258.
19 S. R. Raga, M.-C. Jung, M. V. Lee, M. R. Leyden, Y. Kato and Y. Qi, Influence of Air Annealing on High Efficiency Planar Structure Perovskite Solar Cells, *Chem. Mater.*, 2015, **27**(5), 1597–1603.
20 L. Huang, Z. Hu, J. Xu, K. Zhang, J. Zhang and Y. Zhu, Multi-step slow annealing perovskite films for high performance planar perovskite solar cells, *Sol. Energy Mater. Sol. Cells*, 2015, **141**, 377–382.
21 D. T. Moore, H. Sai, K. W. Tan, D.-M. Smilgies, W. Zhang and H. J. Snaith, *et al.*, Crystallization Kinetics of Organic–Inorganic Trihalide Perovskites and the Role of the Lead Anion in Crystal Growth, *J. Am. Chem. Soc.*, 2015, **137**(6), 2350–2358.
22 A. T. Barrows, S. Lilliu, A. J. Pearson, D. Babonneau, A. D. F. Dunbar and D. G. Lidzey, Monitoring the Formation of a CH3NH3PbI3–xClx Perovskite during Thermal Annealing Using X-Ray Scattering, *Adv. Funct. Mater.*, 2016, **26**(27), 4934–4942.
23 C. Bi, Y. Shao, Y. Yuan, Z. Xiao, C. Wang and Y. Gao, *et al.*, Understanding the formation and evolution of interdiffusion grown organolead halide perovskite thin films by thermal annealing, *J. Mater. Chem. A*, 2014, **2**(43), 18508–18514.

24 Y. Yang, S. Feng, M. Li, W. Xu, G. Yin and Z. Wang, *et al.*, Annealing Induced Re-crystallization in CH3NH3PbI3−xClx for High Performance Perovskite Solar Cells, *Sci. Rep.*, 2017, **7**, 46724.

25 E. L. Unger, A. R. Bowring, C. J. Tassone, V. L. Pool, A. Gold-Parker and R. Cheacharoen, *et al.*, Chloride in Lead Chloride-Derived Organo-Metal Halides for Perovskite-Absorber Solar Cells, *Chem. Mater.*, 2014, **26**(24), 7158–7165.

26 K. W. Tan, D. T. Moore, M. Saliba, H. Sai, L. A. Estroff and T. Hanrath, *et al.*, Thermally Induced Structural Evolution and Performance of Mesoporous Block Copolymer-Directed Alumina Perovskite Solar Cells, *ACS Nano*, 2014, **8**(5), 4730–4739.

27 S. Lilliu, J. Griffin, A. T. Barrows, M. Alsari, B. Curzadd and T. G. Dane, *et al.*, Grain rotation and lattice deformation during perovskite spray coating and annealing probed in situ by GI-WAXS, *CrystEngComm*, 2016, **18**(29), 5448–5455.

28 H.-C. Liao, C.-S. Tsao, M.-H. Jao, J.-J. Shyue, C.-P. Hsu and Y.-C. Huang, *et al.*, Hierarchical i-p and i-n porous heterojunction in planar perovskite solar cells, *J. Mater. Chem. A*, 2015, **3**(19), 10526–10535.

29 L. Oesinghaus, J. Schlipf, N. Giesbrecht, L. Song, Y. Hu and T. Bein, *et al.*, Toward Tailored Film Morphologies: The Origin of Crystal Orientation in Hybrid Perovskite Thin Films, *Adv. Mater. Interfaces*, 2016, **3**(19), DOI: 10.1002/admi.201600403.

30 J. Schlipf, P. Docampo, C. J. Schaffer, V. Körstgens, L. Bießmann and F. Hanusch, *et al.*, A closer look into two-step perovskite conversion with X-ray scattering, *J. Phys. Chem. Lett.*, 2015, **6**(7), 1265–1269.

31 W. Zhang, M. Saliba, D. T. Moore, S. K. Pathak, M. T. Hörantner and T. Stergiopoulos, *et al.*, Ultrasmooth organic–inorganic perovskite thin-film formation and crystallization for efficient planar heterojunction solar cells, *Nat. Commun.*, 2015, **6**, DOI: 10.1038/ncomms7142.

32 T. Miyadera, Y. Shibata, T. Koganezawa, T. N. Murakami, T. Sugita and N. Tanigaki, *et al.*, Crystallization Dynamics of Organolead Halide Perovskite by Real-Time X-ray Diffraction, *Nano Lett.*, 2015, **15**(8), 5630–5634.

33 M. Saliba, T. Matsui, J.-Y. Seo, K. Domanski, J.-P. Correa-Baena and M. K. Nazeeruddin, *et al.*, Cesium-containing triple cation perovskite solar cells: improved stability, reproducibility and high efficiency, *Energy Environ. Sci.*, 2016, **9**(6), 1989–1997.

34 D. Bi, W. Tress, M. I. Dar, P. Gao, J. Luo and C. Renevier, *et al.*, Efficient luminescent solar cells based on tailored mixed-cation perovskites, *Sci. Adv.*, 2016, **2**(1), DOI: 10.1126/sciadv.1501170.

35 L. M. Pazos-Outón, M. Szumilo, R. Lamboll, J. M. Richter, M. Crespo-Quesada and M. Abdi-Jalebi, *et al.*, Photon recycling in lead iodide perovskite solar cells, *Science*, 2016, **351**(6280), 1430–1433.

36 D. K. Mohamad, B. G. Freestone, R. Masters, M. Reinhardt, S. Canning and C. Rodenburg, *et al.*, Optimized organometal halide perovskite solar cell fabrication through control of nanoparticle crystal patterning, *J. Mater. Chem. C*, 2017, **5**(9), 2352–2359.

37 T. Baikie, Y. Fang, J. M. Kadro, M. Schreyer, F. Wei and S. G. Mhaisalkar, *et al.*, Synthesis and crystal chemistry of the hybrid perovskite $(CH_3NH_3)PbI_3$ for solid-state sensitised solar cell applications, *J. Mater. Chem. A*, 2013, **1**(18), 5628–5641.

38 C. C. Stoumpos, C. D. Malliakas and M. G. Kanatzidis, Semiconducting Tin and Lead Iodide Perovskites with Organic Cations: Phase Transitions, High Mobilities, and Near-Infrared Photoluminescent Properties, *Inorg. Chem.*, 2013, **52**(15), 9019–9038.

39 Q. Chen, H. Zhou, T.-B. Song, S. Luo, Z. Hong and H.-S. Duan, *et al.*, Controllable Self-Induced Passivation of Hybrid Lead Iodide Perovskites toward High Performance Solar Cells, *Nano Lett.*, 2014, **14**(7), 4158–4163.

40 R. Brenes, D. Guo, A. Osherov, N. K. Noel, C. Eames and E. M. Hutter, *et al.*, Metal Halide Perovskite Polycrystalline Films Exhibiting Properties of Single Crystals, *Joule*, 2017, **1**(1), 155–167.

41 A. Dualeh, P. Gao, S. I. Seok, M. K. Nazeeruddin and M. Grätzel, Thermal Behavior of Methylammonium Lead-Trihalide Perovskite Photovoltaic Light Harvesters, *Chem. Mater.*, 2014, **26**(21), 6160–6164.

42 W. Zhang, V. M. Burlakov, D. J. Graham, T. Leijtens, A. Osherov and V. Bulović, *et al.*, Photo-induced halide redistribution in organic–inorganic perovskite films, *Nat. Commun.*, 2016, **7**, 11683.

43 Y. Tian, M. Peter, E. Unger, M. Abdellah, K. Zheng and T. Pullerits, *et al.*, Mechanistic insights into perovskite photoluminescence enhancement: light curing with oxygen can boost yield thousandfold, *Phys. Chem. Chem. Phys.*, 2015, **17**(38), 24978–24987.

44 G. Divitini, S. Cacovich, F. Matteocci, L. Cinà, A. Di Carlo and C. Ducati, In situ observation of heat-induced degradation of perovskite solar cells, *Nat. Energy*, 2016, **1**, 15012.

45 A. D. Sheikh, R. Munir, M. A. Haque, A. Bera, W. Hu and P. Shaikh, *et al.*, Effects of High Temperature and Thermal Cycling on the Performance of Perovskite Solar Cells: Acceleration of Charge Recombination and Deterioration of Charge Extraction, *ACS Appl. Mater. Interfaces*, 2017, **9**(40), 35018–35029.

46 S. Karuppuchamy, M. Iwasaki and H. Minoura, Electrochemical properties of electrosynthesized TiO_2 thin films, *Appl. Surf. Sci.*, 2006, **253**(5), 2924–2929.

47 S. Karuppuchamy, K. Nonomura, T. Yoshida, T. Sugiura and H. Minoura, Cathodic electrodeposition of oxide semiconductor thin films and their application to dye-sensitized solar cells, *Solid State Ionics*, 2002, **151**(1–4), 19–27.

48 C. Kvarnström, H. Neugebauer, S. Blomquist, H. J. Ahonen, J. Kankare and A. Ivaska, In situ spectroelectrochemical characterization of poly(3,4-ethylenedioxythiophene), *Electrochim. Acta*, 1999, **44**(16), 2739–2750.

49 N. Sakai, Z. Wang, V. M. Burlakov, J. Lim, D. McMeekin and S. Pathak, *et al.*, Controlling Nucleation and Growth of Metal Halide Perovskite Thin Films for High-Efficiency Perovskite Solar Cells, *Small*, 2017, **13**(14), 1–8.

50 S. Lilliu, T. G. Dane, M. Alsari, J. Griffin, A. T. Barrows and M. S. Dahlem, *et al.*, Mapping Morphological and Structural Properties of Lead Halide Perovskites by Scanning Nanofocus XRD, *Adv. Funct. Mater.*, 2016, **26**(45), 8221–8230.

51 S. Lilliu, M. Alsari, O. Bikondoa, J. Emyr Macdonald and M. S. Dahlem, Absence of Structural Impact of Noble

Nanoparticles on P3HT:PCBM Blends for Plasmon-Enhanced Bulk-Heterojunction Organic Solar Cells Probed by Synchrotron GI-XRD, *Sci. Rep.*, 2015, **5**, 10633.
52 https://youtu.be/ZSUug00lsyU.
53 https://youtu.be/ZSUug00lsyU#t=2m17s.
54 https://youtu.be/ZSUug00lsyU#t=3m07s.
55 https://youtu.be/ZSUug00lsyU#t=3m33s.
56 https://youtu.be/ZSUug00lsyU#t=4m09s.
57 https://youtu.be/ZSUug00lsyU#t=4m58s.
58 https://youtu.be/ZSUug00lsyU#t=6m07s.
59 https://youtu.be/ZSUug00lsyU#t=6m48s.
60 https://youtu.be/ZSUug00lsyU#t=7m09s.
61 https://youtu.be/ZSUug00lsyU#t=10m05s.